Development of a spatio-temporal acoustic pressure measurement technique utilizing background oriented schlieren technique

S. Ichihara[1,*], M. Yamagishi[2], A. Ishibashi[1,*], Y. Kurashina[1], M. Ota[2], Y. Tagawa[1]

1: Dept. of Mechanical Systems Engineering, Tokyo University of Agriculture and Technology, Japan
2: Dept. of Engineering, Chiba University, Japan
*Corresponding author: s226020x@st.tuat.ac.jp

Keywords: BOS, Fast checker demodulation, Vector tomography, Acoustic pressure field.

ABSTRACT

We proposed an image and optical-based technique to measure the spatio-temporal acoustic pressure field using our established BOS technique instead of the hydrophone. In this proposed BOS technique, fast checker demodulation (FCD) was used as a displacement detection method, and vector tomography (VT) was used as an axisymmetric tomography. The hydrophone, a direct measurement method commonly used for pressure wave measurement, has the disadvantage of disturbance the flow field. In the experiments, focused ultrasound was measured using two types of hydrophones with different diameters ($1\,\mathrm{mm}$ and $2\,\mathrm{mm}$) and BOS, and the temporal-pressure values were compared. BOS successfully captured the temporal evolution of the focused ultrasound field (spatial resolution: $1.0\,\mu\mathrm{m}$) at a frequency of $4.554\,\mathrm{MHz}$ in water, including the sound field reflected by the scatterer (hydrophone). The two types of hydrophones measured different amplitudes for the same target depending on their diameter. This discrepancy is attributed to the lower spatial resolution of the hydrophones compared to the wavelength of the ultrasound ($329\,\mu\mathrm{m}$) under the experimental conditions. In terms of temporal-pressure values, BOS exhibited systematic errors when the pressure was amplified. Therefore, synthetic data were used to investigate the measurement limits of displacement in FCD. The results revealed that the issue of underestimating displacement, which cannot be explained by the criteria proposed by Wildeman (2018), could be defined by the integrated power spectra of distorted image. BOS, using FCD and VT, can measure the sound field, including reflected waves, with high spatiotemporal resolution. Additionally, FCD requires criteria to avoid underestimating the displacement field when measuring continuous pressure waves.

1. Introduction

Ultrasound is utilized in various field, such as medical, treatment, and engineering fields. For example, drug delivery systems (DDS) use ultrasound to induce cavitation within the drug-containing droplets, causing them to collapse and deliver the drug to the affected area. In DDS, improving the control of ultrasound within the droplets can enhance the therapeutic effect (Orita et al., 2023).

For a long time, hydrophones have been commonly used to measure the temporal and spatial characteristics of a ultrasound field (Xing et al., 2021). However, a hydrophone disturbs the flow field and consumes a high computational cost to measure the field distribution. In addition, it might malfunction due to the cavitation when it is used to measure high power ultrasound field. Therefore, non-contact and efficient ultrasound field measurement technique is of interest and optical and image-based techniques is expected to solve these problems.

Background-oriented schlieren (BOS) technique which uses only a camera and a background image is one of these optical and image-based technique. BOS has an easier experimental setup than schlieren (Koponen et al., 2019) and phase contrast techniques (Harigane et al., 2013), thus having few restrictions on the experimental method. Moreover, the sensitivity and spatial resolution of BOS can be simply optimized according to the characters of the ultrasound filed by adjusting the distance between the target and the background image, and the properties of the camera. In the case of phase contrast techniques, the effects of diffraction cannot be ignored at large amplitudes or high frequencies. Therefore, only ultrasound with amplitudes below $0.1\,\mathrm{MPa}$ and frequencies below $20\,\mathrm{MHz}$ can be measured(Goldfain et al., 2021; Nakamura et al., 2018).

In this paper, we proposed an image and optical based technique to measure the spatio-temporal acoustic pressure field using our established BOS technique, which indicates Fast checker demodulation(FCD) as a displacement detection method(Shimazaki et al., 2022) and vector tomography(VT) as an axisymmetry tomographic technique(Ichihara et al., 2022), instead of the hydrophone. The measurement results are compared and discussed with those measured using hydrophones of different effective diameters. Furthermore, we discuss the criteria for FCD when using synthetic displacement fields, by varying the background pattern, amplitude, and wavelength.

2. Theory

2.1. Background-oriented schlieren technique

The principle of the BOS technique is illustrated in Fig. 1. The background and the object are placed along the optical axis as shown in Fig. 1, where the pressure field is calculated from the captured images. When the refractive index of a fluid changes, an apparent displacement (vector field) appears on the background. This displacement of the captured images in x-direction u is proportional to the density gradient $\partial\rho/\partial x$ integrated along the optical axis and can be expressed as follows (van Hinsberg & Rösgen, 2014; Ichihara et al., 2022):

$$u = \frac{Z_D}{n_0}\int_{Z_D-\Delta Z_D}^{Z_D+\Delta Z_D}\frac{\partial n}{\partial x}dz = \frac{KZ_D}{n_0}\int\frac{\partial \rho}{\partial x}dz, \tag{1}$$

where n is the refractive index of measurement target, n_0 is the refractive index of surrounding fluid, Z_D is the distance from the center of the measurement target to the background image, ΔZ_D is the thickness of the density gradient, and K is the Gladstone-Dale constant. Gladstone-Dale relation is established using the refractive index and density (Raffel, 2015)

$$n = \rho K + 1. \tag{2}$$

Section 2.2 explains the calculation of the integrated density gradient and the density field. After obtaining the density field, the pressure field is calculated using the Tait equation,

$$\frac{p + B}{p_0 + B} = \left(\frac{\rho}{\rho_0}\right)^{\alpha}. \tag{3}$$

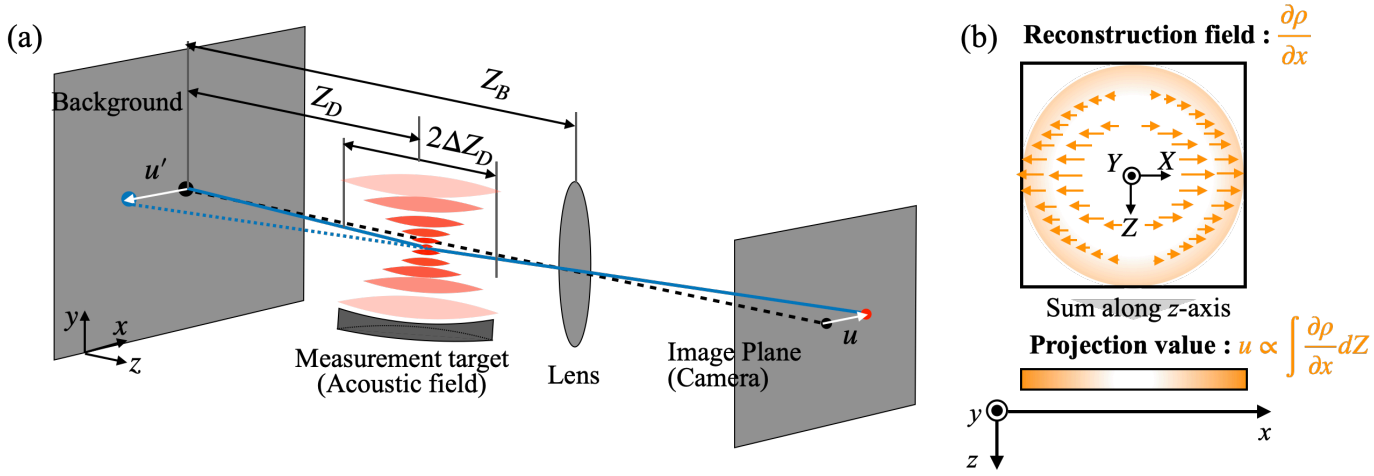

Figure 1. (a) Principle of BOS technique. (b) The reconstruction (density gradient) distribution and projection value (displacement value) of a certain xz cross section viewed from the y-axis direction.

2.2. Vector tomography

The measurement target (reconstructed distribution) and displacement field (integrated value) shows Cartesian coordinates (x, y, z) in Fig. 1(a) while Fig. 1(b) shows the reconstructed distribution and integrated value at a certain $x - z$ cross-section along the y-axis. Herein, reconstruction distribution is indicated using the Cartesian coordinates with capital letters (X, Y, Z) which has the origin at center of the reconstructed distribution. The coordinates (x, y, z) is connected to the coordinates (X, Y, Z) using constant value C like a $x = X + C1$, $y = Y + C2$, $z = Z + C3$.

The density gradient field $\partial\rho/\partial x$ of the measurement target is defined as an symmetrical object around the Y-axis thus it is a point reflection on $x - z$ cross-section with only radial components. The $\partial\rho/\partial x$ of Eq. 1 can be indicated $\partial\rho/\partial r \cos\theta$ as using polar coordinates (r, θ) through the relations with Cartesian coordinates (X, Z), where $X = r\cos\theta$ and $Z = r\sin\theta$. When the coordinates of

integrated value u and reconstructed distribution $\partial\rho/\partial x$ are linearly correlated, these component indicated on the same X-axis. Therefore integrated components of Eq. 1 is

$$u(X) \propto \int_{-\Delta Z_D}^{\Delta Z_D} \frac{\partial}{\partial x}\rho\left(\sqrt{X^2+Z^2}\right) \cdot \frac{X}{\sqrt{X^2+Z^2}} dZ. \tag{4}$$

The Cartesian coordinates (X, Z) is replaced with the Cartesian coordinates $(\bar{x}, \bar{z})$ where values exist only at equally spaced grid points (herein, referred to as discretization). Both share the same origin. The displacement $u(\bar{x})$ at $\bar{x}$ of Eq. 4 is discretized using $\partial\rho/\partial r$ and coefficient $\alpha_{\bar{x},\bar{z}} \propto \bar{x}/\sqrt{\bar{x}^2+\bar{z}^2}\,(=\cos\theta_{\bar{x},\bar{z}})$

$$u(\bar{x}) \propto \Sigma_{\bar{z}=-\Delta Z_D}^{\Delta Z_D} \alpha_{\bar{x},\bar{z}} \frac{\partial}{\partial x}\rho\left(\sqrt{\bar{x}^2+\bar{z}^2}\right). \tag{5}$$

The constant coefficient $\alpha_{i,\bar{z}}$ depend on the ΔZ_D. Since the other displacement u at coordinate $\bar{x}$ can be similarly described, the displacement matrix $\boldsymbol{u}$ will be expressed as a multiplication of constant matrix $\boldsymbol{A}$ and density gradient matrix along r-direction $\partial\boldsymbol{\rho}/\partial r$,

$$\boldsymbol{u} = \frac{KZ_D}{n_0}\boldsymbol{A}\frac{\partial\boldsymbol{\rho}}{\partial r}. \tag{6}$$

where Eq. 6 shows the relationship between the displacement matrix $\boldsymbol{u}$ and the density gradient matrix $\partial\boldsymbol{\rho}(r)/\partial r$ at a certain $y = y_0$. The density gradient in the radial-direction is calculated from the constant matrix $\boldsymbol{A}$ of Eq. 6 where the density gradient field has the value of $Y - r$ cross-section which contains Y-axis, the axis of symmetry. Therefore, density field can be calculated by integrating the $\partial\rho/\partial r$ along r-axis,

$$\rho = \int_0^{\inf} \frac{\partial\rho}{\partial r} dr, \tag{7}$$

where the boundary condition in Eq. 7 set up as a hydrostatic fluid pressure.

3. Experiments

Figure 2 (a) shows the experiment setup. In a tank filled with pure water, a transducer is placed at the bottom and a background image with $20\,\mu\mathrm{m}$ checkered pattern is placed $21.0\,\mathrm{mm}$ from the center of the focused ultrasound. A current with a sinusoidal wave of $4.554\,\mathrm{MHz}$ is generated using a multifunction generator and amplified by an amplifier before receiving by the transducer to generate the focused ultrasound. By using a delay generator, the transducer is synchronized with a laser and a high-resolution camera (EOS R5, Canon, 5,000 $\times$ 8,000 pixels, Shutter speed $0.5\,\mathrm{s}$). As shown in Fig. 2 (b), once the transducer is started, the camera immediately starts recording while the laser light starts illuminating after a delay time, which is initially set as $t = 32.000\,\mu\mathrm{s}$. The illumination lasts $10\,\mathrm{ns}$ for the camera to capture the background image with the underwater ultrasound. After that, the delay generator starts the camera and the laser again but not the

transducer to capture the background image without the underwater ultrasound. With these the two captured images, the displacement field can be calculated using FCD (Shimazaki et al., 2022; Wildeman, 2018). Fig. 3 (a) shows the background image captured by camera one without and the other without the ultrasound. The cycle are repeated for 100 times, thus 100 sets of images are used to calculate the averaged displacement values. Fig. 3 (b) shows 100 times averaged displacement result detected by FCD. The same 100 cycles are repeated for 45 times where each time the laser delay time t is increased by an interval of $15\,\mathrm{ns}$.

Two different types of hydrophones (Muller-platte Needle Probe and Onda HNR-0500, hereinafter called hydrophone(Muller) and hydrophone(Onda), respectively) were placed at the center of focused ultrasound facing the transducer to measure the pressure fluctuation from $t = 32.000\,\mu\mathrm{s}$. For comparison with the pressure field measured by BOS in the presence of the hydrophones, the values measured by BOS are averaged over a region of $1.5 \times 250^2\pi\ \mu\mathrm{m}^3$ and $1.5 \times 500^2\pi\ \mu\mathrm{m}^3$(hereinafter referred to as BOS(Muller) and BOS(Onda), respectively).

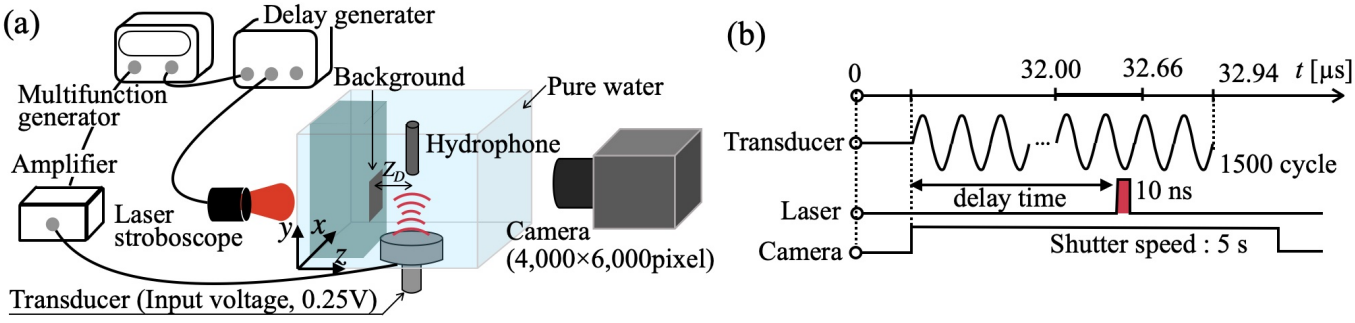

Figure 2. (a) Experimental setup. (b) Signal transmitted from function generator to transducer, laser light, and camera.

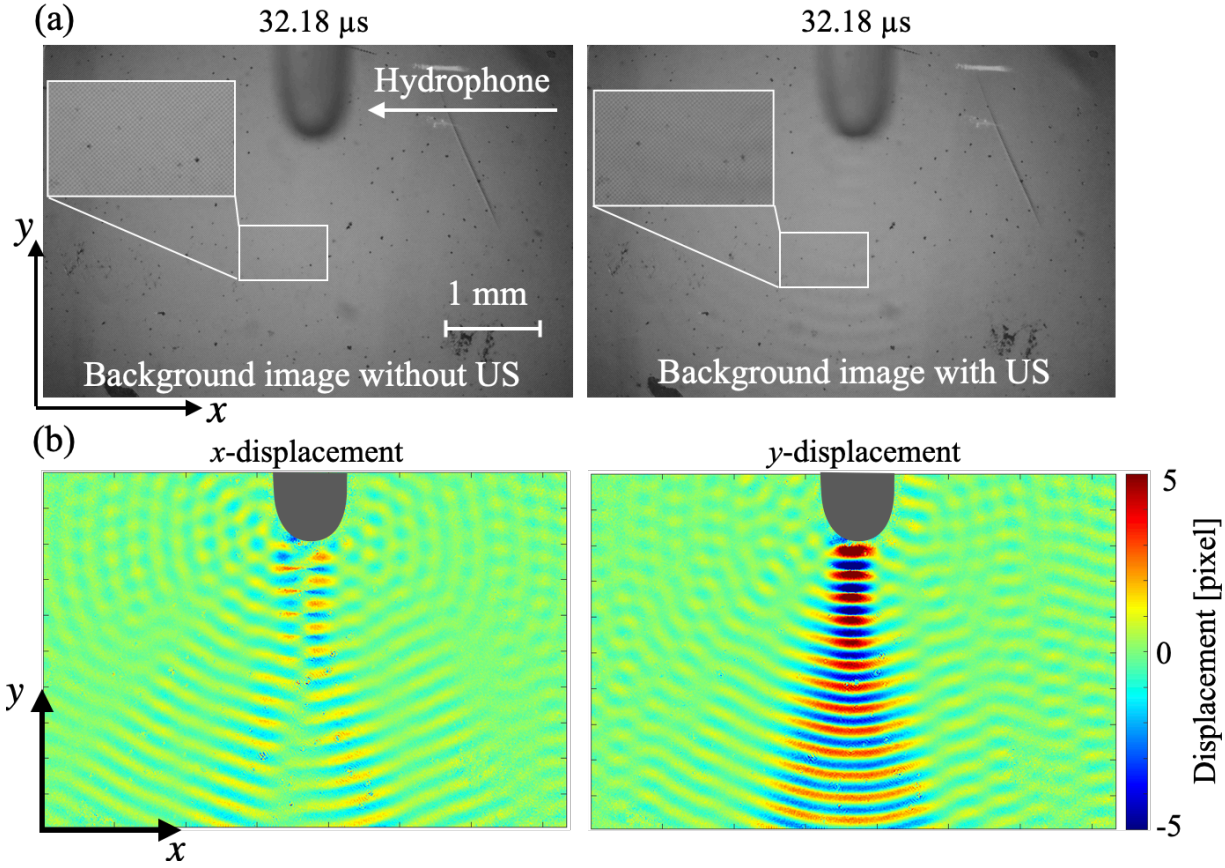

Figure 3. (a) The background image without and with the measurement target, which is the focused ultrasound. (b)The displacement fields calculated by FCD. Left: x-displacement, Right: y-displacement.

4. Result

Figure 4 shows the pressure fields with the hydrophones measured using BOS at the delay times of 32.180, 32.510, and 32.645 µs, respectively. BOS visualized the different wave distributions at each time, successfully capturing the propagating pressure field of focused ultrasound. When comparing the acoustic fields of the same delay time between muller and onda, there is a clear difference in the pressure distribution, specifically the maximum pressure value of onda is higher than that of muller. This is likely due to the differences in the tip shape and diameter of hydrophone.

In the pressure field measured by BOS, the spatial average values are plotted in Fig. 5. The red and blue markers show pressure measured by BOS(Muller) and BOS(Onda), respectively. The pink and light blue rigid lines show the pressure values measured by hydrophone(Muller) and hydrophone(Onda), respectively. For each delay time, the temporal distribution of the pressure is measured using the hydrophone for 5 times, thus error bar represents the maximum and minimum value from the 225 data-set. The pressure trend of BOS(Muller) and BOS(Onda) are in good agreement with hydrophone(Muller) and hydrophone(Onda) result. In short, both hydrophones

measured the spatio averaged pressure value where is related to the effective diameter of hydrophone. Harris (1985) indicated that if half of the effective diameter of a hydrophone is larger than the wavelength of measurement target, the hydrophone measures the spatio averaged pressure value (Harris, 1985). In this experiment, the spatial resolution of the BOS and hydrophone are $1.0\,\mu\mathrm{m}$ and $500\,\mu\mathrm{m}$, respectively. Therefore, under the conditions of this experiment, BOS could ignore the effects of spatial averaging effect compared to the hydrophone, achieving quantitative measurement of the acoustic field with high spatial resolution.

The amplitude of BOS(Muller) is smaller than that of hydrophone(Muller) in Fig. 5. There are two possible reasons for this: limitation of displacement detection method and calculation error in BOS. The limitation of displacement detection method is discussed in Section 5. In the calculation step of BOS, pressure gradient was calculated from the displacement result, and integral computation is necessary to estimate the pressure value from pressure gradient. In this experiment, we assume that the boundary condition is hydrostatic pressure. Therefore, estimation value involves the amplitude. Whereas the overestimated error related to the experimental error.

In terms of the amplitude, negative pressure value of BOS(Onda) is in good agreement with hydrophone(Onda) in Fig. 5. On the other hand, the positive pressure values measured by BOS(Onda) are larger than those measured by the hydrophone(Onda). This difference is related to the fact that the error bar of the hydrophone(Onda) at the maximum pressure, which is around $0.25\,\mathrm{MPa}$, is larger than that of the hydrophone (Muller), which is around $0.11\,\mathrm{MPa}$. This error bar caused by the oscillation where the ultrasound hit the hydrophone. Then, the pressure field measured by BOS around the antinode of time versus pressure, experiences slight phase change in the same delay time conditions. In short, the overestimated error at BOS(Onda) is attributed to the experimental error.

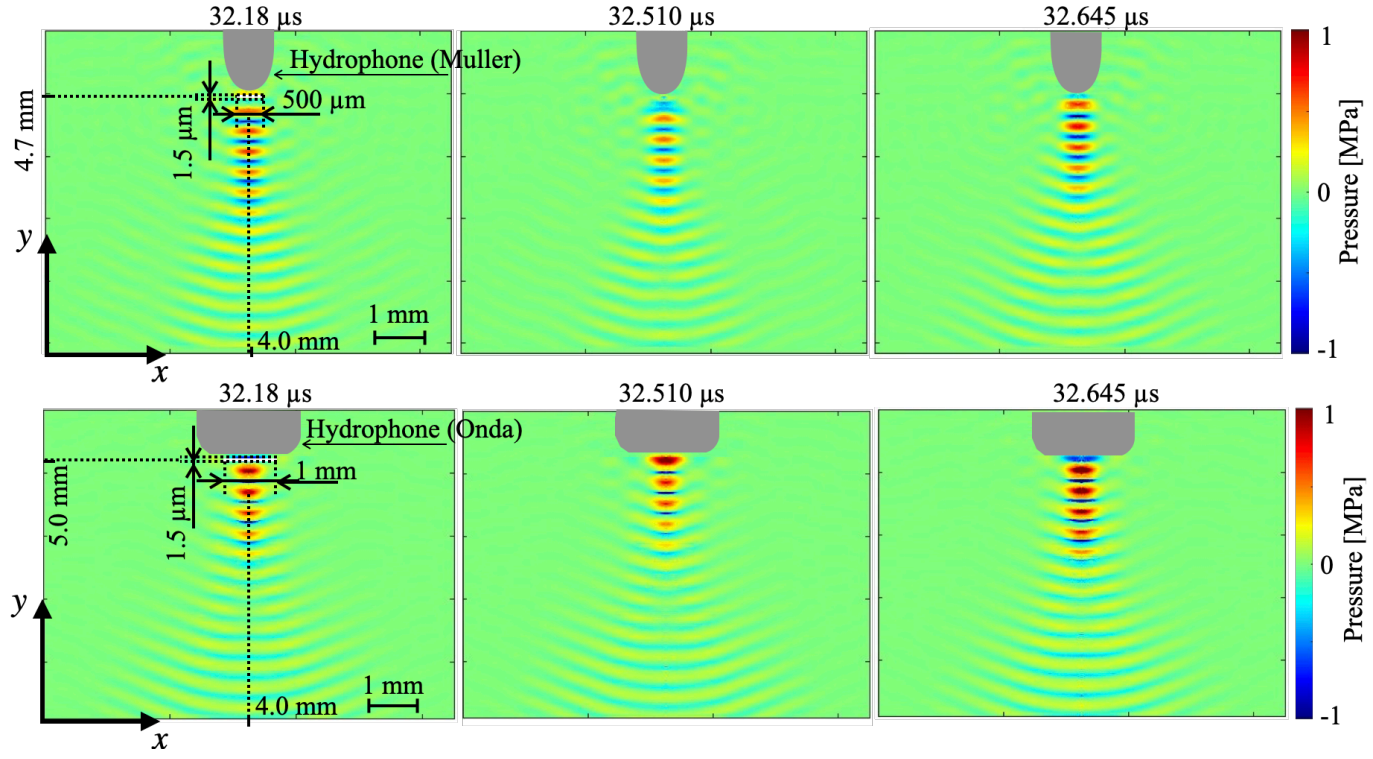

Figure 4. The top and bottom images show the pressure field including the muller hydrophone and onda hydrophone measured by BOS, respectively.

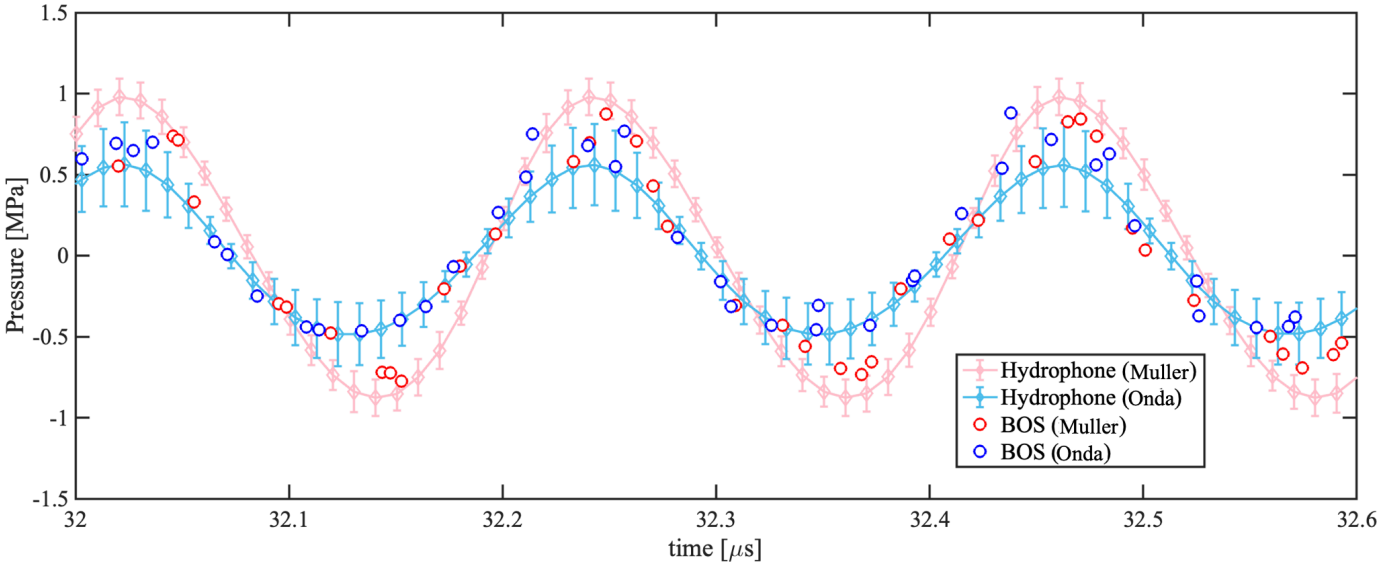

Figure 5. Time vs pressure measured by BOS and hydrophone.

5. The criteria in FCD

Even when the criteria presented by Wildeman (2018) and Shimazaki et al. (2022) are met, displacement detection using FCD encounters issues under certain conditions where displacement cannot be accurately detected. The temporal pressure data in Fig. 5 where the measurements of the hydrophone and BOS do not match were affected by the aforementioned influences. In this section, we discuss specific conditions using synthetic reference images and distorted images, while meeting the criteria presented by Wildeman (2018).

5.1. Synthetic data

Figure 6 (a) shows the reference image and distorted image. The reference pattern forms

$$I_0(\boldsymbol{r}) = \frac{1}{2} + \frac{1}{4}\left(\cos\left(\frac{2\pi}{w}\boldsymbol{k_1}\cdot\boldsymbol{r}\right) + \cos\left(\frac{2\pi}{w}\boldsymbol{k_2}\cdot\boldsymbol{r}\right)\right), \tag{8}$$

where $\boldsymbol{r}$ denotes pixel coordinates (x, y), w denotes the wavelegth of the reference pattern, and in this condition $\boldsymbol{k_1} \perp \boldsymbol{k_2}$ and $|\boldsymbol{k_1}| = |\boldsymbol{k_2}|$. In k-space, Fig. 6 (b) shows the relationship between the orthogonal wavenumber vectors k_1 and k_2.

The distortion is represented by a sine wave

$$u(\boldsymbol{r}) = A_p \sin\left(2\pi\frac{\boldsymbol{r}}{\lambda}\right), \tag{9}$$

which is centered at the origin of the reference image. Here, A_p [pixels] denotes the amplitude , and λ [pixels] denotes the wavelength of the distortion. Fig. 6 (c) shows the displacement field determined by FCD from reference image I_0 and distortion image I. The reference and distorted image I_0, I are squares of 250 pixels.

Based on the methods for creating reference and distorted images, we analyzed a total of 72 conditions using FCD, with w set to 5, 10, 15, 20, 25, and 30 pixels, A_p set to 1, 2, 3, and 4 pixels, λ set to 30, 40, and 50 pixels. Additionally, k_1 and k_2 were set to (1,0) and (0,1), respectively. However, conditions that do not satisfy the criteria presented by Wildman to prevent aliasing artifacts and phase wrapping, such as

$$k_s < \frac{k_{rad}}{\sqrt{2}}, \tag{10}$$

$$k_s u_s < \frac{1}{\sqrt{2}}, \tag{11}$$

$$k_c u_s < \pi, \tag{12}$$

were excluded from the analysis results. Here, k_s indicates the wavenumber related to the distortion, k_{rad} indicates the wavenumber determined by the reference image, and u_{max} indicates the maximum displacement.

5.2. Discussion

Figure 7 shows the displacement field along the x-axis at $y = 0$, with all conditions satisfying the criteria of Eqs. 10, 11, and 12. Comparing the original displacement calculated from Eq. 9 with the displacement calculated by FCD from the reference and distorted images, they almost match in Fig. 7 (a). However, in Fig. 7(b), the FCD underestimates the amplitude compared to the original one. Comparing Figs. 7(a) and (b), when the wavelength w of the reference image and the wavelength λ of the distortion are equal, the issue of FCD underestimation occurs with the increase in amplitude A_p. The threshold amplitude A_p for the FCD underestimation issue varies with the wavelength w and λ. Therefore, the criteria presented by Wildeman (2018) do not hold when considering the amplitude A_p, the wavelength w, and the wavelength λ.

Figure 8 shows the integrated power spectra within a radius k_{rad} around the carrier peak at k_1 in k-space for all conditions. The horizontal axis represents the wavelength w of the pattern of reference image. From Fig. 8, it can be observed that regardless of the wavelength λ or amplitude A_p of the distortion, the integrated power spectra decrease and approach the value of the reference pattern as the wavelength w increases. Additionally, when the wavelengths λ, w of the distortion and the reference image remain constant, the integrated power spectra decrease more significantly with lower amplitudes A_p. The orange dashed line indicates the boundary where the FCD underestimation issue occurs, based on the analysis results from Fig. 7. This dashed line shows that if the integrated power spectra exceed this line, the FCD underestimates the displacement compared to the original. Consequently, using the integrated power spectra, we can determine the optimal threshold for the reference image in wave distortion measurement. In this experiment, the BOS results could have been affected by the underestimation issue caused by FCD.

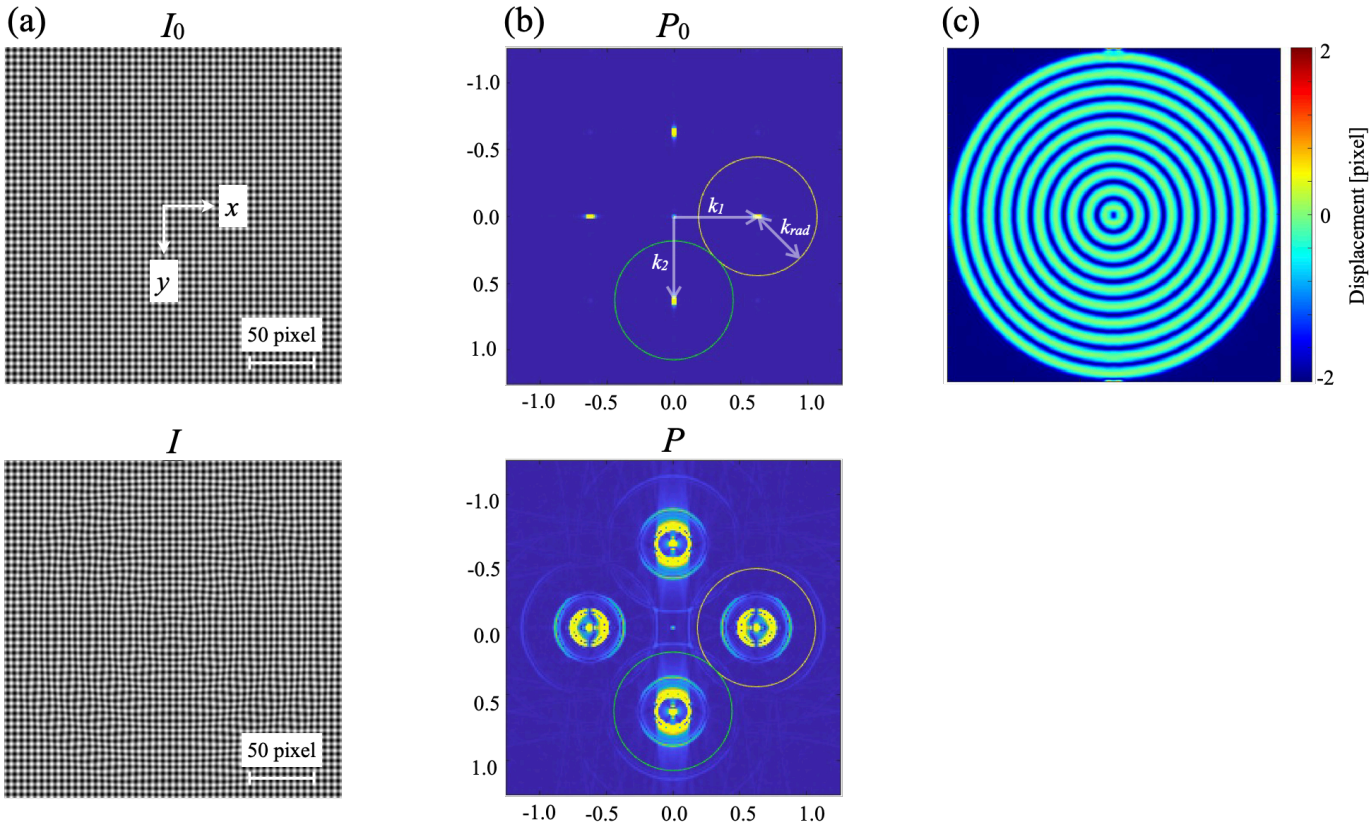

Figure 6. The displacement detection method using FCD. (a) The top image shows the reference image with a wavelength $\lambda = 40\,\mathrm{pixels}$, and the bottom image shows the distorted image with distortion. (b) indicates the intensity of the power spectra P_0, P in k-space. The top image shows the k-space result of the Fourier transform of the reference image I_0, while the bottom image shows the k-space result of the Fourier transform of the distorted image I. k_{rad} is the radius of a circle. (c) illustrates the displacement calculated by FCD using the power spectra P_0 and P.

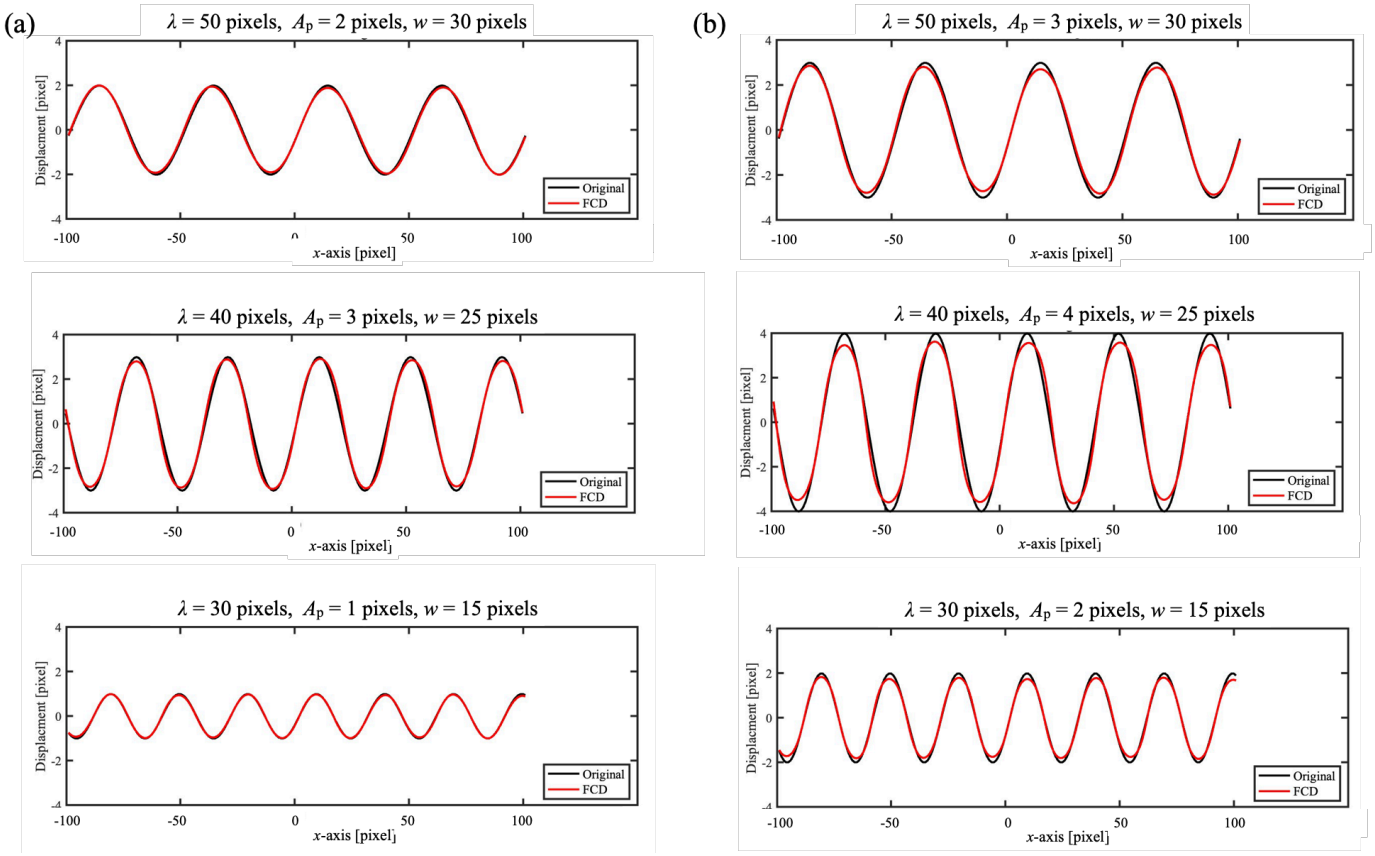

Figure 7. The displacements along the x-axis at $y = 0$. The black solid line represents the original displacement applied to the background image I, while the red solid line represents the displacement calculated by FCD from the background images I_0 and I. (a) shows the condition where the original and the FCD displacement are almost identical, while (b) shows the condition where they do not match.

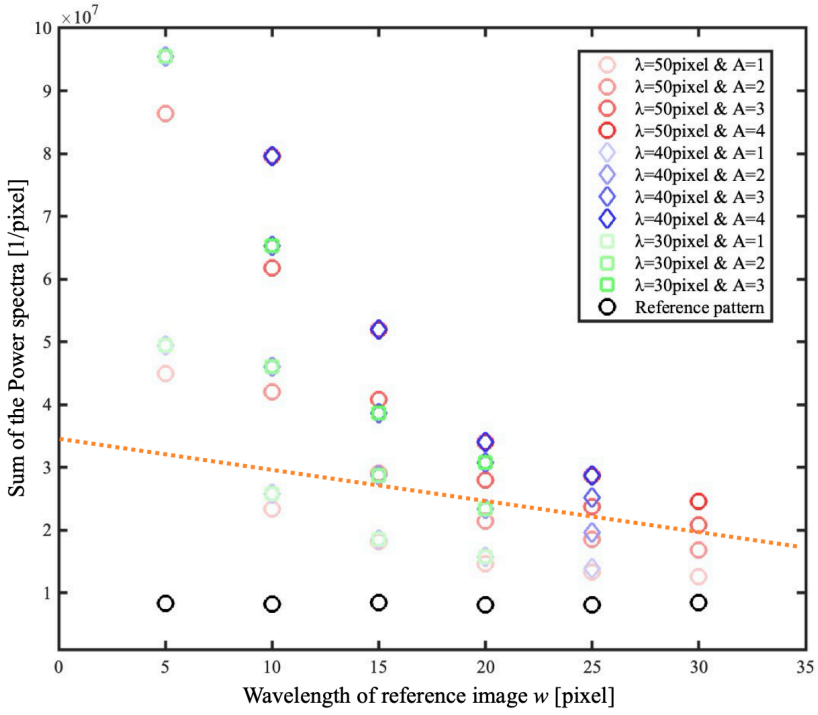

Figure 8. shows the integrated power spectra within a radius k_{rad} around the carrier peak at k_1 in k-space for all conditions, relative to the wavelength w of the reference image. The red, blue, and green plots represent the results for distortion wavelengths of 50, 40, and 30 pixels, respectively. The black plot shows the integrated power spectra of the reference image. The orange line indicates the boundary where there is a discrepancy in amplitude between the displacement calculated by FCD and the original displacement calculated from Eq. 9.

6. Conclusions

In this paper, we proposed a non-contact spatio-temporal acoustic pressure field measurement technique instead of hydrophone. We compared the pressure value focused ultrasound of about $4.554\,\mathrm{MHz}$ measured using BOS and hydrophones of different diameter. The pressure distribution measured by BOS captured the effects of the reflection wave which are related to the tip shape and diameter of hydrophone. In terms of temporal distribution, wave trend of BOS and hydrophone measurement result are in good agreement and amplitudes are different between both hydrophones. The BOS result was spatially averaged according to the effective diameter of each hydrophone, thus the difference in amplitude was caused by that the spatially averaged pressure value measured by the hydrophone. Although these BOS measurement result contains error which is related to the limitation of the displacement detection method. By using synthetic reference images and distorted images, we identified error factors that cannot be eliminated by the criteria proposed byWildeman (2018). Furthermore, by utilizing the integrated power spectra of the distorted images, we proposed criteria that account for amplitude, wavelength, and back-

ground pattern in waveform measurement.

In short, our BOS technique can measure a high spatio-temporal acoustic pressure field.

Acknowledgements

This work was supported by JSPS KAKENHI Grant Numbers JP23KJ0859, JP23H01600, JP24H00289, the HEIWA NAKAJIMA Foundation, International Academic Collaborative Grant, and JST PRESTO Grant Number JPMJPR21O5, Japan.

References

Goldfain, A. M., Yung, C. S., Briggman, K. A., & Hwang, J. (2021). Optical phase contrast imaging for absolute, quantitative measurements of ultrasonic fields with frequencies up to 20 mhz. *The Journal of the Acoustical Society of America*, *149*(6), 4620–4629.

Harigane, S., Miyasaka, R., Yoshizawa, S., & Umemura, S.-i. (2013). Optical phase contrast mapping of highly focused ultrasonic fields. *Japanese Journal of Applied Physics*, *52*(7S), 07HF07.

Harris, G. R. (1985). A discussion of procedures for ultrasonic intensity and power calculations from miniature hydrophone measurements. *Ultrasound in medicine & biology*, *11*(6), 803–817.

Ichihara, S., Shimazaki, T., & Tagawa, Y. (2022). Background-oriented schlieren technique with vector tomography for measurement of axisymmetric pressure fields of laser-induced underwater shock waves. *Experiments in Fluids*, *63*(11), 182.

Koponen, E., Leskinen, J., Tarvainen, T., & Pulkkinen, A. (2019). Acoustic pressure field estimation methods for synthetic schlieren tomography. *The Journal of the Acoustical Society of America*, *145*(4), 2470–2479.

Nakamura, T., Iwasaki, R., Yoshizawa, S., & Umemura, S.-i. (2018). Quantitative measurement of ultrasonic pressure field using combination of optical phase contrast and nonlinear acoustic holography methods. *Japanese Journal of Applied Physics*, *57*(7S1), 07LB13.

Orita, Y., Shimanuki, S., Okada, S., Nakamura, K., Nakamura, H., Kitamoto, Y., … Kurashina, Y. (2023). Acoustic-responsive carbon dioxide-loaded liposomes for efficient drug release. *Ultrasonics Sonochemistry*, *94*, 106326.

Raffel, M. (2015). Background-oriented schlieren (bos) techniques. *Experiments in Fluids*, *56*, 1–17.

Shimazaki, T., Ichihara, S., & Tagawa, Y. (2022). Background oriented schlieren technique with fast fourier demodulation for measuring large density-gradient fields of fluids. *Experimental Thermal and Fluid Science*, *134*, 110598.

van Hinsberg, N. P., & Rösgen, T. (2014). Density measurements using near-field background-oriented schlieren. *Experiments in fluids*, *55*, 1–11.

Wildeman, S. (2018). Real-time quantitative schlieren imaging by fast fourier demodulation of a checkered backdrop. *Experiments in Fluids*, *59*(6), 97.

Xing, G., Wilkens, V., & Yang, P. (2021). Review of field characterization techniques for high intensity therapeutic ultrasound. *Metrologia*, *58*(2), 022001.